In-situ irradiation tolerance investigation of high strength ultrafine tungsten-titanium carbide alloy

El Atwani, Osman
Cunningham, W. Stret
Esquivel, Erika V.
Li, Meimei
trelewicz, Jason
Uberuaga, Blas P.
Maloy, Stuart Andrew

To be published in: Acta Materialia

DOI to publisher's version: 10.1016/j.actamat.2018.10.038

In-situ Irradiation Tolerance Investigation of High Strength Ultrafine Tungsten-Titanium Carbide Alloy

O. El-Atwani[1*], W.S. Cunningham[2], E. Esquivel[1], M. Li[3], J.R. Trelewicz[2,4], B. P. Uberuaga[1], S.A. Maloy[1]

[1]Materials Science and Technology Division, Los Alamos National Laboratory, Los Alamos, NM, USA
[2]Department of Materials Science and Chemical Engineering, Stony Brook University, Stony Brook, NY, USA
[3]Division of Nuclear Engineering, Argonne National Laboratory, Argonne, IL, USA
[4]Institute for Advanced Computational Science, Stony Brook University, Stony Brook, NY, USA

Abstract

Refining grain size and adding alloying elements are two complementary approaches for enhancing the radiation tolerance of existing nuclear materials. Here, we present detailed in-situ irradiation research on defect evolution behavior and irradiation tolerance of ultrafine W-TiC alloys (thin foils) irradiated with 1 MeV Kr^{+2} at RT and 1073 K, and compare their overall performance to pure coarse grained tungsten. Loop Burgers vector was studied confirming the presence of <100> loops whose population increased at high temperature. Loop density, average loop area, and overall damage are reported as a function of irradiation dose revealing distinct defect evolution behavior from pure materials. The overall damage generally followed the average loop size trend, which decreased with time for both temperatures, but was higher at 1073 K and attributed to biased vacancy sink behavior of the TiC dispersoids evidenced by large vacancy clusters on their interfaces. By comparison, the overall loop and void damage in pure tungsten was larger by a factor of six and two, respectively. The improved irradiation damage resistance in the alloys is thus attributed to the effect of dispersoids in 1) the enhancement in annihilating defects and mutual defect recombination due to both dispersoids and a higher grain boundary density; 2) decreasing the loop mobility, causing shrinkage and annihilation of loop density, which was confirmed via in-situ video. Several mechanisms are illustrated to describe the performance of the complex alloy system. The results motivate further experimental and modeling research that aims to understand the many different phenomena occurring at different time scales

Keywords: tungsten alloy, ultrafine, electron microscopy, dislocation loops, Burgers vector, irradiation tolerance

* Corresponding author: oelatwan25@gmail.com

1. Introduction

Owing to its high melting temperature, high thermal conductivity, and resistance to sputtering, tungsten is considered to be the primary choice as a plasma facing material in fusion reactors [1, 2]. Under such applications, tungsten will be exposed to high doses of low energy helium ($10\text{-}10^4$ eV) and 14.1 MeV neutron irradiation of approximately hundreds of displacements per atom (dpa) over an anticipated 3-5 year lifetime [3, 4]. The damage resulting from this exposure will be in the form of interstitial loops, dislocations, vacancy clusters, helium bubbles, and cavities [5-9]. Among the suggested routes to reduce the detrimental effects of irradiation induced defects is the introduction of defect sinks. Grain boundaries are known to act as sinks and can enhance the annihilation of irradiation-induced defects.[10-12] Nanocrystalline (NC) and ultrafine-grained (UFG) materials with their high grain boundary fraction have been reported to have improved radiation tolerance in both BCC and FCC metallic materials as well as ceramic materials.[5, 13-21] . In addition, nanocrystalline metals and alloys have been found to have superb strength and have shown a transition from dislocation-mediated to grain boundary-mediated deformation as well as a tendency for shear localization [22].

Traditionally, most tungsten and tungsten alloy parts are produced by powder processing and high temperature sintering followed by thermomechanical processing (usually hot rolling) to increase density and ductility. This production route generally results in tungsten with a grain size (typically) ranging from 10-20 microns. Moreover, tungsten produced this way is susceptible to embrittlement if placed in operating temperatures above its recrystallization temperature. In order to obtain ultrafine grained or nanocrystalline tungsten alternative methods have to be pursued. In particular, severe plastic deformation (SPD) of the bulk sintered product, or alternatively SPD of the bulk surface layer, represents one potential approach [23, 24]. SPD of bulk material from equal channel angular pressing (ECAP) [23], high pressure torsion [24] or a combination thereof

[25] have been used successfully to produce UFG as well as nanocrystalline tungsten. Surface deformation has also been successful at producing UFG on tungsten surface layers by plane strain extrusion machining [26] and surface mechanical attrition [27]. However, in an irradiation context, while the high density of sinks is desirable to eliminate radiation-induced defects, nanocrystalline materials are only metastable and prone to radiation-induced grain growth, eventually reducing or eradicating the very characteristic that made them advantageous.

Advanced powder processing techniques such as mechanical alloying can be used to obtain nanocrystalline tungsten with alloying additions that can result in stabilization of the nanocrystalline state via grain boundary segregation, as reported by Chookajorn et al. [28]. Stable nanocrystalline tungsten alloys have also been realized through thin film deposition techniques, such as magnetron sputtering, where their exceptional thermal stability was attributed to heterogeneous solute distributions inhibiting microstructural coarsening [29]. In materials produced through powder processing, aggressive milling of the powders with spherical media [30] in an inert (Ar) or reducing (H_2) atmosphere [31] often introduces small oxide or carbide impurities, which can also contribute to impeding grain growth through grain boundary pinning. Tungsten samples alloyed with small additions of TiC (ranging from 0.2 to 1.1 weight percentage) have been developed by this fabrication route [31-36]. Significant improvements include increased recrystallization temperature, gains in fracture strength over pure tungsten (when milled under H_2 atmosphere) [36], and increased tensile elongation of the alloyed over the unalloyed tungsten samples when tested at elevated temperatures above 1773 K [37]. These improvements are attributed to reduced grain size and increased grain boundary strength of the alloys. The thermal conductivity of W-TiC (at 0.5 wt%) exhibited only a marginal temperature dependence and was generally reduced at low temperatures relative to pure tungsten but comparable at higher temperature due to the temperature dependence of unalloyed tungsten. The alloys also had an inferior response to thermal shock loading versus unalloyed tungsten, though improvements have been achieved through grain boundary sliding based microstructural modification (GSMM) [33].

Based on its promising mechanical behavior and improved resistance to recrystallization embrittlement, tungsten alloyed with small amounts of TiC have been investigated as a potential radiation-tolerant material. This study aims to contribute further to the knowledge of these alloys by presenting the findings of in-situ-irradiation on as-HIPed W with 1.1 wt% TiC. We report on the starting microstructure and Vickers hardness of the W-1.1 wt% TiC. Microstructural evolution during irradiation, including loop density, average loop size, and overall damage, is reported as a function of displacement per atom (dpa) during 1 MeV Kr^{++} irradiation at room temperature (RT) and 1073 K. The loop Burgers vector type is reported at both temperatures and void damage is studied at 1073 K. The results are compared to coarse-grained tungsten irradiated at 1075 K under the same irradiation conditions. The differences observed in the overall damage evolution and irradiation tolerance between the W -1.1 wt% TiC sample and the pure coarse- grained tungsten, which can only be observed in-situ, provides new insights on the role of alloying elements and nano dispersoids in the enhanced irradiation tolerance of the W-TiC alloys.

2. Experimental

2.1. Sample Preparation

Tungsten with 1.1 wt% TiC addition was obtained as hot isostatically pressed to 1 GPa at 1620K where the TiC powders were milled in a hydrogen environment; further details of the powder milling and processing can be found in ref. [31]. This sample is referred to as W-TiC (1.1%). We note that due to the powder milling process, the alloy contained 5-6 wt% molybdenum, though with complete miscibility. Three millimeter diameter discs were cut from the sample through electrical discharge machining and subsequently ground and polished using standard metallographic techniques. Microhardness testing was performed on a Durascan unit using a 200 g load. A coarse grained tungsten (CGW) sample purchased form ESPI Metals, US was used to compare the results of the W-TiC (1.1%) sample to pure tungsten.

For in-situ analysis, the discs were ground to approximately 80 micron thickness. The W-TiC (1.1%) samples were electropolished in a Tenupol-5 using a solution of 200 mL sulfuric acid (H_2SO_4) and 800 mL ethanol (C_2H_5OH) at -10 ^{0}C. The CGW sample was electropolished using 0.5 % NaOH/water solution at RT. For texture characterization, electron backscattered diffraction (EBSD) was performed with an average indexing value was ~ 0.8. Cross section imaging was performed using focused ion beam (FIB).

2.2. In-situ Experiments

Thinned samples approximately 100 nm thick were irradiated in-situ in the intermediate voltage electron microscope (IVEM) with a 300 keV electron beam attached to a Tandem accelerator at Argonne National Laboratory. Prior to the in-situ experiment, the samples were annealed in-situ inside the transmission electron microscope (TEM) using a Gatan Heating holder at 1123 K. Irradiations were then performed at RT and 1073 K using 1 MeV Kr^{+2}. The average dose rate was approximately 0.000075 dpa.s^{-1} and the total dose was 2 dpa. The dpa values were calculated using the Kinchin-Pease model in the Stopping Range of Ions in Matter (SRIM) Monte Carlo computer code (version 2013) [38] where 40 eV [39] was taken as the displacement threshold. The Kr^{+2} and damage distributions in the sample are given in Figure S1 in the supplemental. A CCD camera with 4k x 4k resolution was used to capture video and still images at different dpa values.

2.3. Defect Analysis

2.3.1. Loop Burgers vector

To determine the Burgers vector of the loops in the irradiated samples, loops were imaged under two-beam conditions with <110> and <200> g vectors using an FEI-Tecnai-G2-F30 TEM with electron beam energies of 300 keV in the Electron Microscopy Laboratory (EML) at LANL. In BCC materials, 1/2<111> and <100> Burgers vectors can form with a total of seven possibilities: $1/2\langle 111\rangle$, $1/2\langle\bar{1}11\rangle$, $1/2\langle 1\bar{1}1\rangle$, $1/2\langle 11\bar{1}\rangle$, <100>, <010>, and <001>. With <200> g vector imaging, 5 different possibilities (all <111> Burgers vector and one <100> Burgers vector) are visible and using the <110> g vector, 4 different possibilities are visible (two of each Burgers vector type). Therefore, the type of the Burgers vector present was obtained by solving two equations with two unknowns as detailed below.

2.3.2. Defect density, area, and total damage

To determine the total average loop density and area, ten grains within multibeam conditions (where all loops can be visible), were chosen to minimize quantification error in measuring loop densities (since loops are invisible at g.b = 0). For ten different dpa values, the loop density in every grain was determined following the method presented in ref. [40]. The average of all loop densities in the grains was then obtained by taking the average of loop densities in the ten individual grains. Similarly, loop areas were measured from the ten different grains to minimize errors in average loop area due to different g.b contrast. To determine the total damage, the product of loop density and average loop area was taken. Void density and area was determined in a similar way using Fresnel under-focus images (under-focus value was 1.5 µm) where voids appear bright. It should be noted that quantification errors in loop measurements can occur due to image forces, glissile prismatic loop gliding to the surface, and changes in foil thickness across the sample [41]. All quantification, however, was performed on grains that were adjacent to each other within the same sample thickness (~ 100 nm). The above factors can affect absolute values but not trends, and in this work, focus is placed on comparison of the overall trends. Details about the quantification method are given in [19, 42].

3. Results

3.1. Pre-irradiation microstructure

The microstructure of the as-received W-TiC (1.1%) consisted of equiaxed grains as observed in Figures 1 (TEM and FIB cross-sectional image) and 2 (EBSD) with an average grain size of ~ 290 nm placing it in the ultra-fine (100-500 nm) grain size regime. A large fraction of the boundaries are high angle grain boundaries (HAGB), see Figure 2(e). The TiC ring reflection is evident in the ring diffraction pattern as is the ring diffraction pattern of tungsten. The TiC nano dispersoids were well distributed, though as evident in Figure 2 (c) some particle clusters were apparent. The vast majority of the TiC particles resided along the grain boundaries though some existed within the grains as well. Vicker's microhardness of the sample in the as-received condition averaged 8 GPa; in contrast, a commercially available pure tungsten sample averaged 4.6 GPa, thus demonstrating the significant improvement in mechanical properties realized through the combination of grain refinement and alloying.

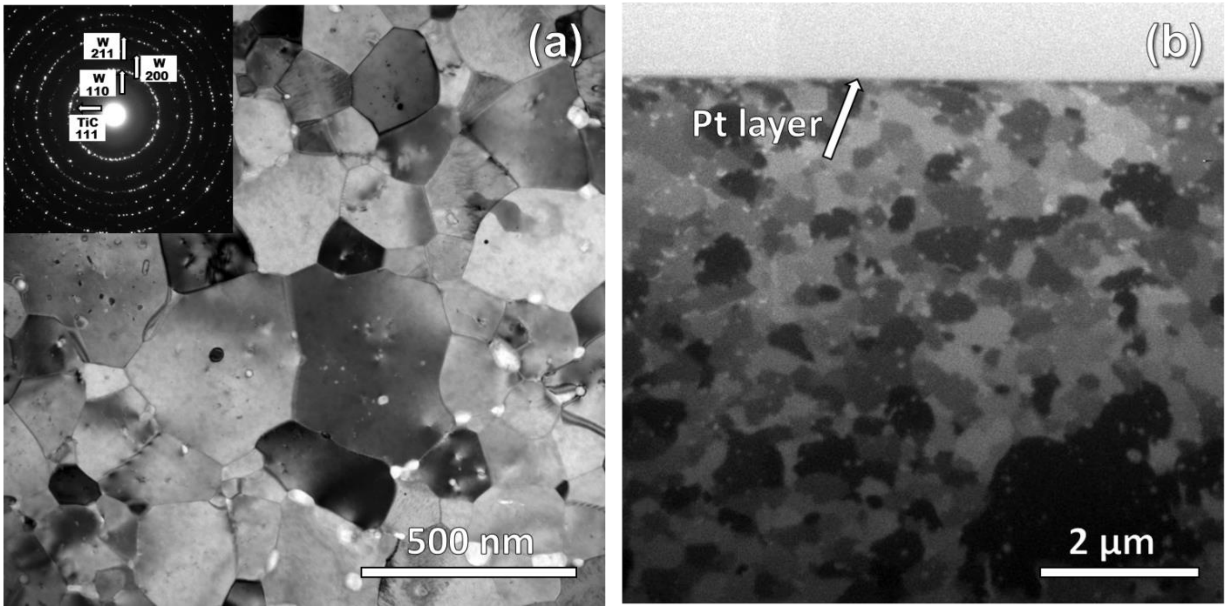

Figure 1: (a) TEM bright-field micrograph of the as-received W-TiC (1.1%) sample showing TiC dispersoids on the grain boundaries as well as the grain matrices. Insert shows the diffraction pattern rings of pure W and TiC dispersoids. (b) Cross-section FIB image (using the secondary electrons of the gallium ion beam) showing no grain size or dispersoid density change with depth.

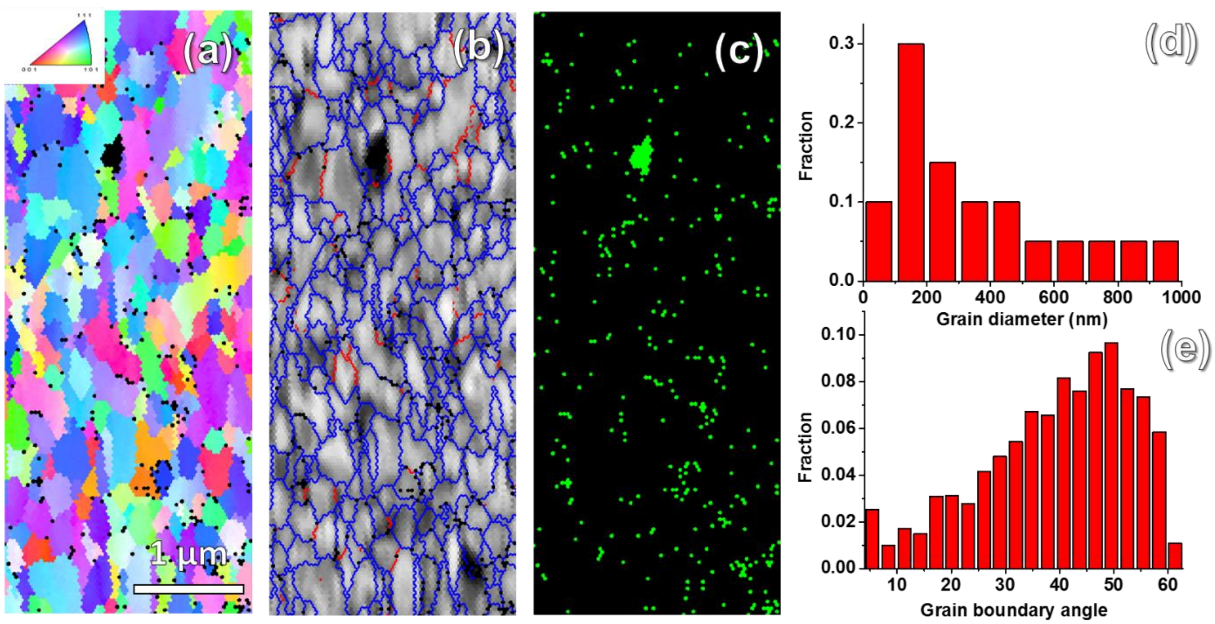

Figure 2: (a) EBSD [001] inverse pole-figure (IPF) map of the W-TiC (1.1%) sample, and (b), (c) the corresponding grain boundary map and TiC phase map, respectively. (d), (e) Average grain size and grain boundary disorientation angle distributions respectively.

3.2. Post-irradiation Loops Burgers Vector Characterization

Part of the scope of this investigation was to characterize the Burgers vector of the dislocation loops formed after irradiation and, in addition, estimate the fraction of glissile <111> loops and sessile <100> loops. The analysis was performed on the samples irradiated to 2 dpa at RT and 1073 K (considered to correspond to stage II and stage IV recovery in tungsten respectively) [6]. Upon tilting to near the [001] zone axis between the g <200> and <100>, both 1/2<111> (in this study analyzed as <111>) and <100> type dislocation loops were visible. Following a procedure similar to Yabuchi et al.[43], Yi et al.[7] and previously used by El-Atwani et al. [42], the percentage of each type of dislocation loop was determined. Using the <200> g vector, four variants of the <111> and one of <100> type are expected, while using the <110> g vector, two variants of <111> and <100> type are possible. The average density of the loops present was calculated at each condition by simultaneously solving Eq. 1a and 1b where *x* represents the density of the <111> variant and *y* the <100> variant:

$$\textbf{\textit{<200> g vector analysis}}\text{:}\quad 4x + 1y = D_{<200>} \tag{1a}$$

$$\textbf{\textit{<110> g vector analysis:}}\quad 2x + 2y = D_{<110>} \tag{1b}$$

where $D_{<200>}$ and $D_{<110>}$ are the average loop densities observed in the 2-beam bright field TEM images using the g <200> and g <110> vectors respectively. Note that the same quantification area, shown in Figure 3 for the samples irradiated at RT and 1073K, was analyzed for both g vector conditions at a given temperature. The percentage of <111> loop variants was estimated to be 44% at RT and 32% at 1073 K confirming the existence <100> loops. Note that a similar trend where the concentration of <111> loops is higher at RT relative to 1073 K was observed by El-Atwani et al.[42] on CGW irradiated to 0.25 dpa (at a dpa rate of 0.0167 dpa.s^{-1}) using 3 MeV Cu ions; the opposite trend was observed on the same CGW when the dpa rate was 0.00167 dpa.s^{-1} .

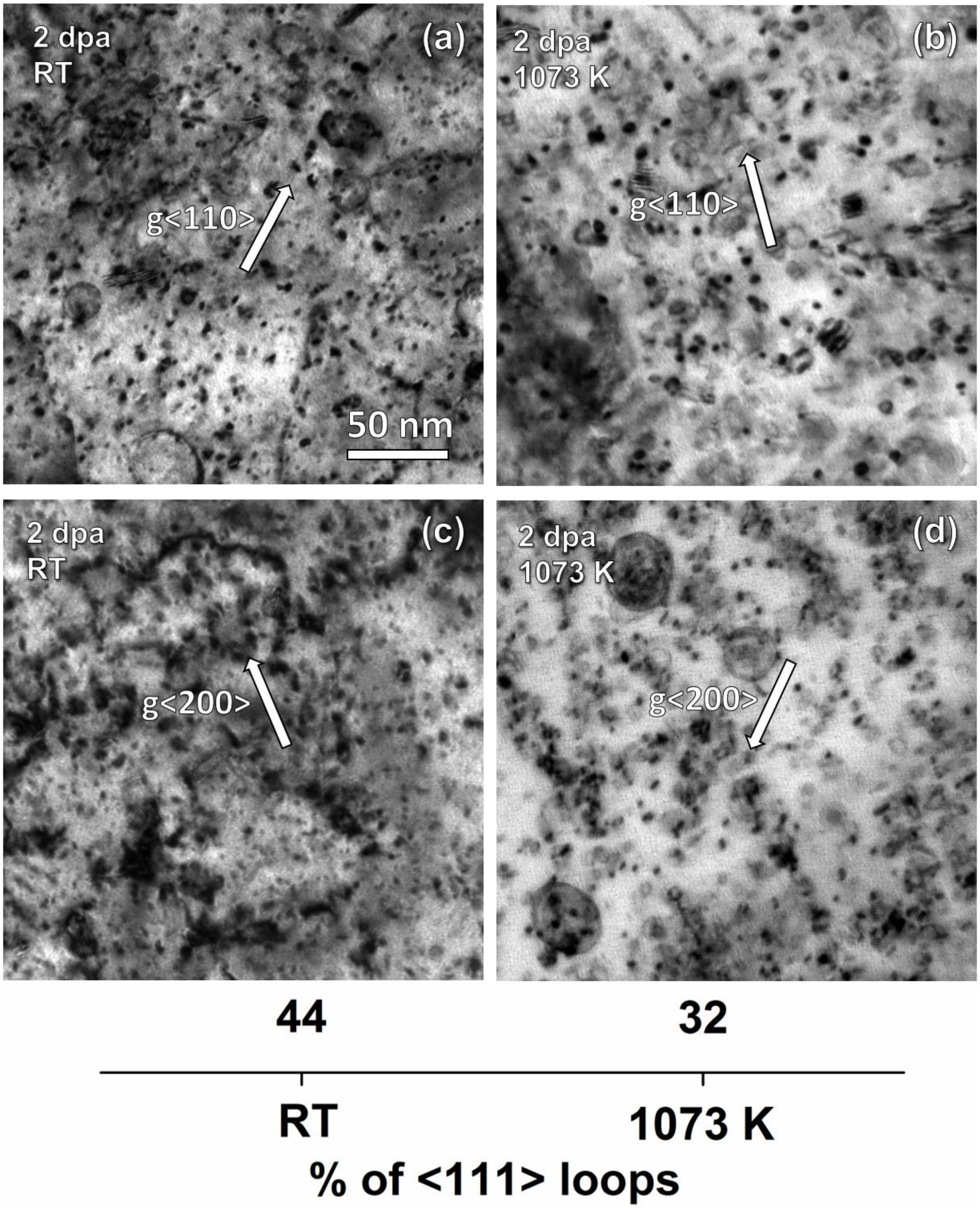

Figure 3: (a), (b) Bright-field 2-beam TEM micrographs using <110> g vector for the *in-situ* 2 dpa 1 MeV Kr^{+2} irradiated W-TiC (1.1%) samples at RT and 1073 K respectively. (c), (d) Bright-field 2-beam TEM micrographs using <200> g vector for the 2 dpa irradiated W-TiC (1.1%) samples at RT and 1073 K respectively. Images are used to determine the percentages of <111>

and <100> Burgers vectors loops (shown at the bottom of the figure) at RT and 1073 K. All micrographs have the same scale bar.

3.3. In-situ morphology and damage quantification

The morphology of the irradiated samples at RT and 1073 K at selected dpa values is shown in Figure 4. For irradiation damage quantification, still images were taken from the in-situ video. From these images, the average loop density and the average size (area) was determined for each dose. From the product of these measurements, an estimate of the total damage was determined and a graphical representation of the results is shown in Figure 5. The loop density in the samples irradiated at RT and 1073 K initially increased, reaching a maximum (within the studied dose range) at approximately 0.5 dpa and 0.4 dpa respectively, followed by a slight decrease and eventual plateauing of the loop density. The average area (size) of the loops appeared to cycle up and down with dose at both temperatures, but at all doses (within the confines of the total dose of this study), was larger at 1073 K. Consequently, the total damage was also higher at all doses for the sample irradiated at the higher temperature (Figure 6).

As expected, voids were observed in the sample irradiated at the elevated temperature of 1073 K as evident in the Fresnel under-focused image shown in Figure 7. The average void density, average void area and change in volume (swelling determined from visible voids) were determined only at the final dose of 2 dpa as the imaging conditions were not favorable for in-situ void quantification. The average void density was measured to be approximately 0.06 nm^{-2}, with an average size (area) of 2.8 nm^2, resulting in 0.22% swelling. The TiC dispersoids exhibited much lower damage relative to the surrounding tungsten grains as shown in Figure 8 with no apparent large loop formation. In addition, no apparent change occurred in the size of the dispersoids during irradiation. However, larger voids (~ 8-16 nm) were observed in the vicinity of the interface between the TiC dispersoids and the tungsten matrix particular for the high temperature irradiation.

3.4. Grain size effect in the ultrafine regime

In order to determine whether there was an effect of grain size on average loop density, size, and damage, measurements were taken from various grains varying in diameter with dose. The results of these measurements are shown in Figure 9. No evident trend is observed with respect to grain size in agreement with previous results on pure tungsten with elongated ultrafine grains irradiated with 3 MeV Cu^{+}.[42] It is also evident from the figure that at the same dose, grains with similar sizes can exhibit different irradiation damage levels, which could be due to different sink strengths of the nearby grain boundaries.

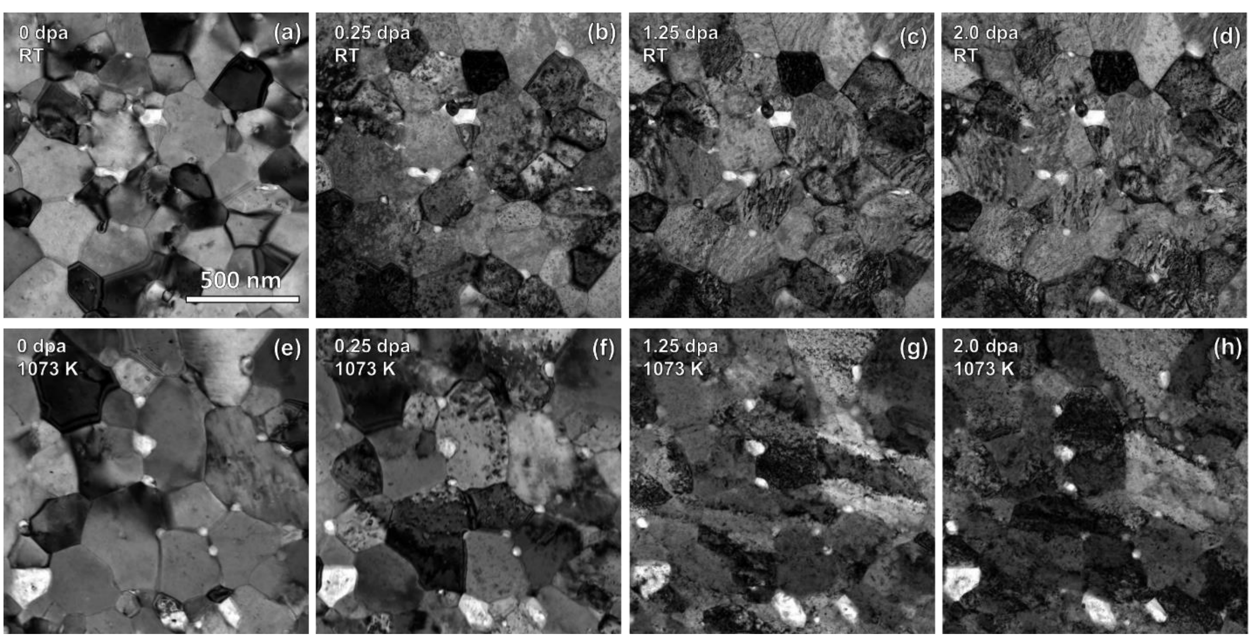

Figure 4: (a), (b), (c), (d) Bright-field TEM micrographs as a function of dpa for *in-situ* 1 MeV Kr^{+2} irradiated W-TiC (1.1%) sample at RT. (e), (f), (g), (h) Bright-field TEM micrographs as

a function of dpa for the *in-situ* 1 MeV Kr^{+2} irradiated W-TiC (1.1%) sample at 1073 K. All micrographs have the same scale bar.

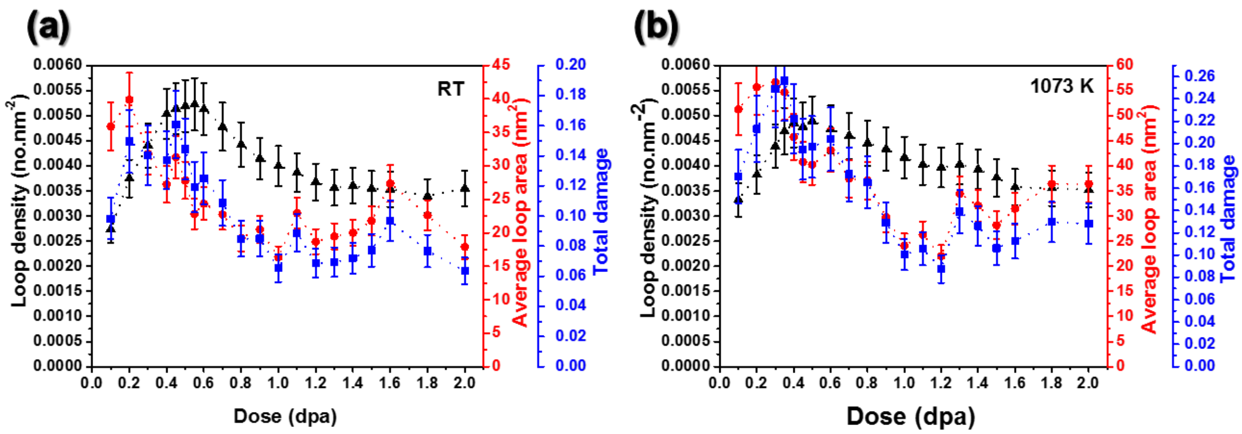

Figure 5: Comparisons of average areal loop density, loop area and total damage (loop density × loop area) as a function of dpa for the *in-situ* 1 MeV Kr^{+2} irradiated W-TiC (1.1%) sample at RT and 1073 K. Error bars are included to reflect errors in quantifying the same area several times. Note that the scales for average loop area and total damage are different in the two figures, with larger scales for the 1073 K irradiation.

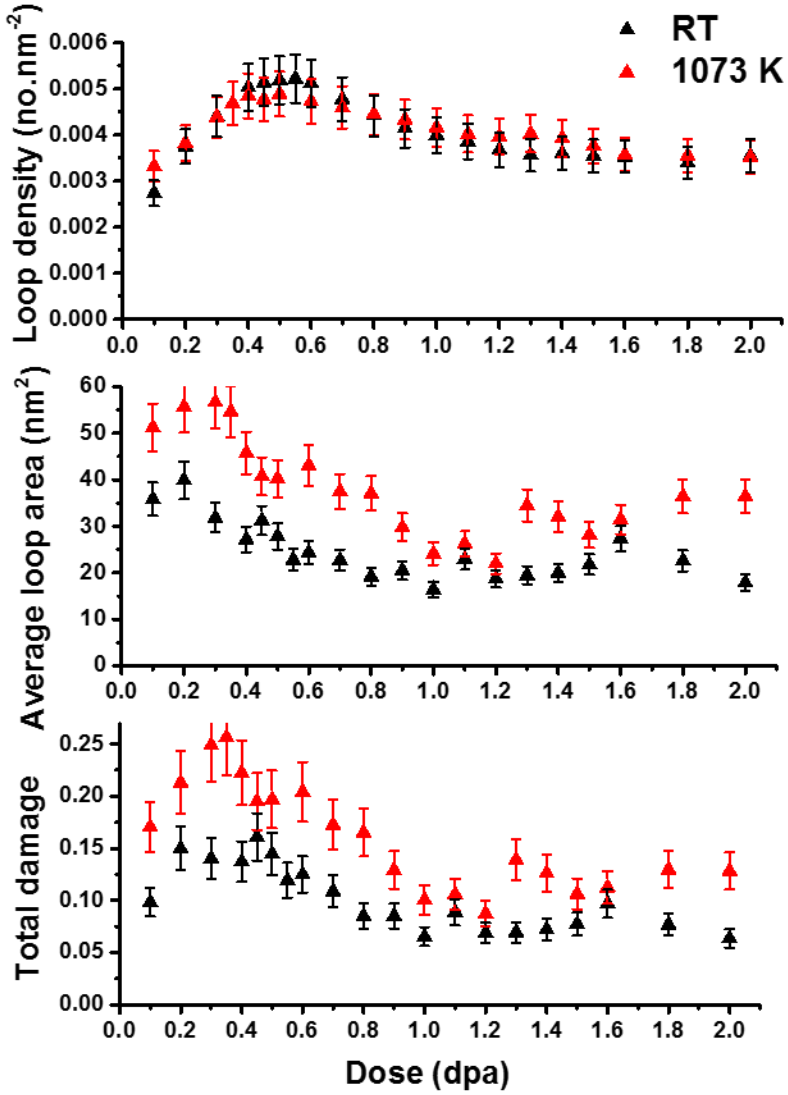

Figure 6: Superimposed average areal loop density, loop area and total damage (loop density × loop area) as a function of dpa for the (a) RT and (b) 1073 K *in-situ* 1 MeV Kr^{+2} irradiated W-TiC (1.1%) sample. Error bars are included to reflect errors in quantifying the same area several times. This is the same data as presented in Figure 5, but with the measurements for the two different temperatures superimposed for easier comparison.

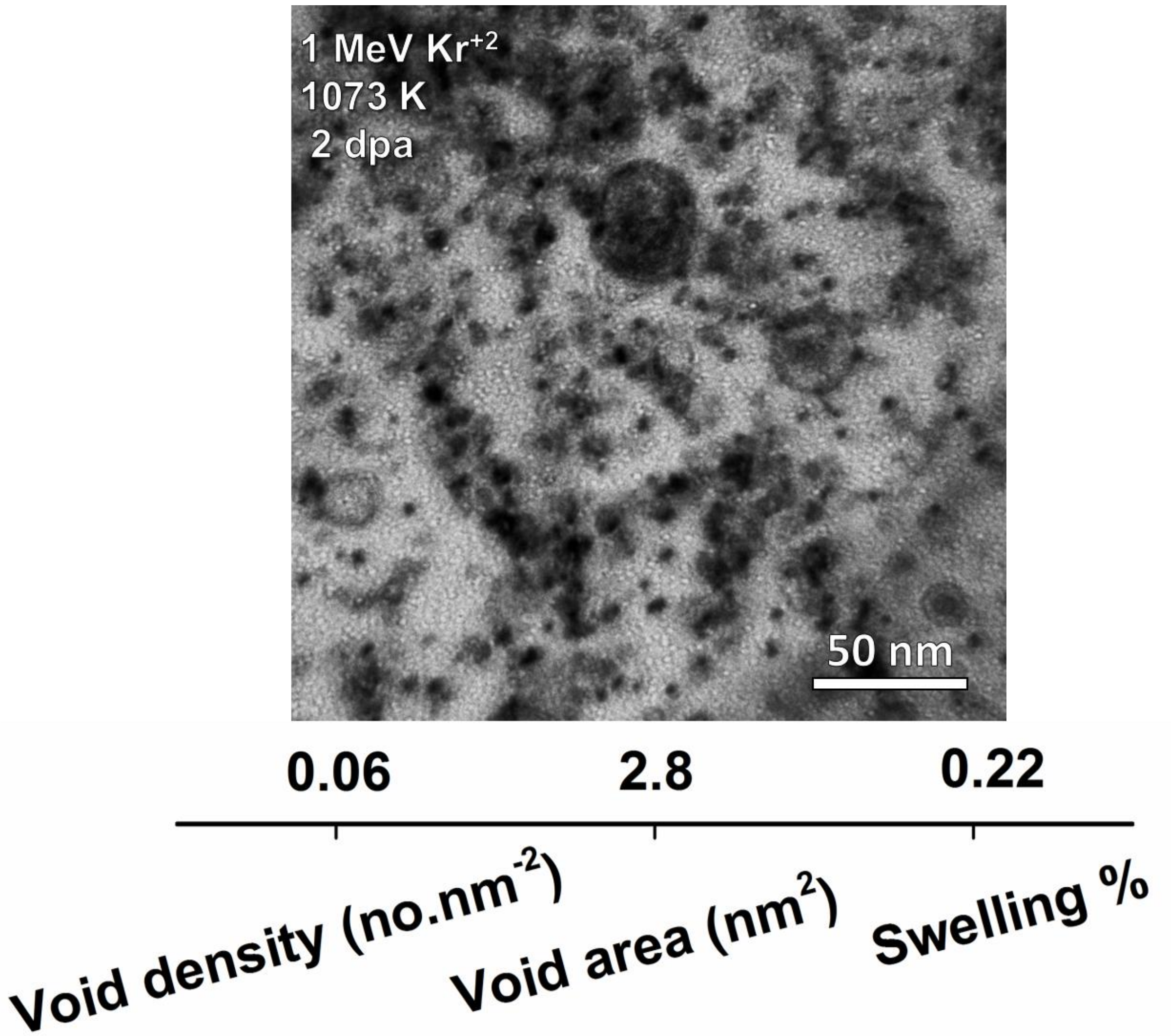

Figure 7: Bright-field Fresnel (underfocus) TEM micrograph of 2 dpa *in-situ* 1 MeV Kr^{+2} irradiated W-TiC (1.1%) sample showing uniform distribution of voids (bright spots in the image). Average void density, void area and the corresponding swelling % extracted from this image are given at the bottom of the figure.

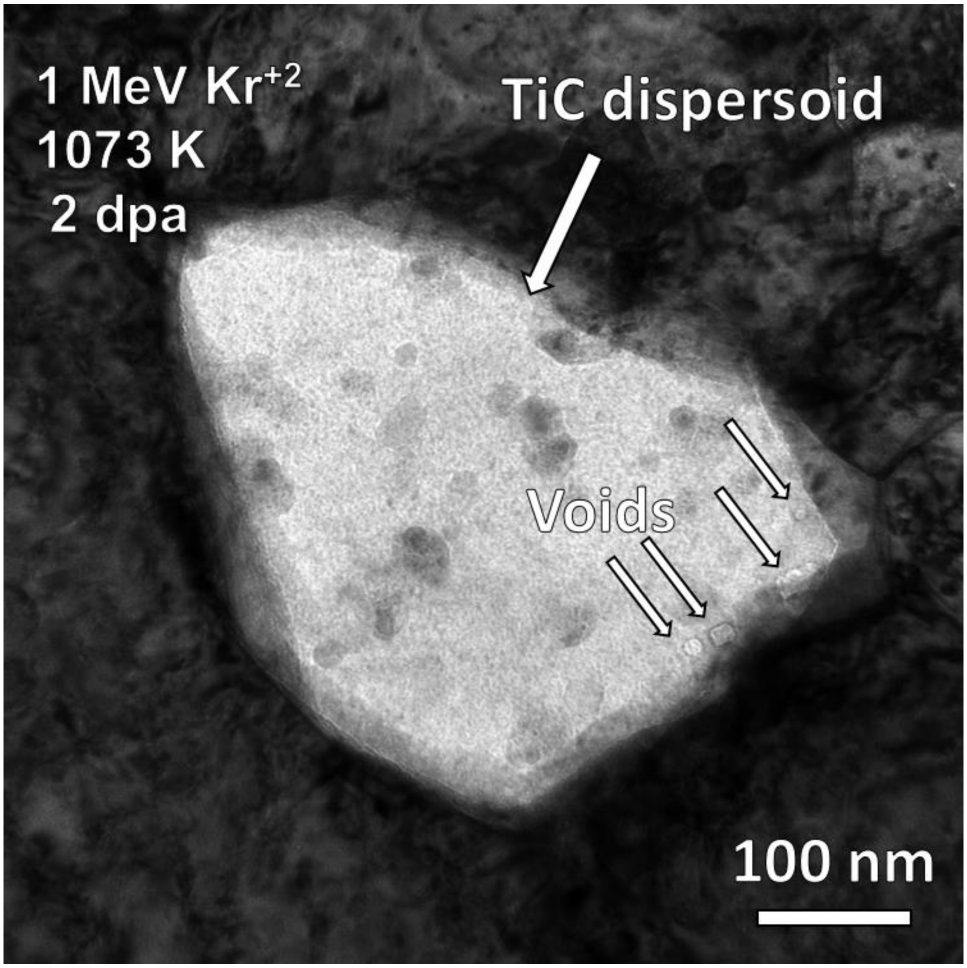

Figure 8: Bright-field TEM micrograph of the 2 dpa *in-situ* 1 MeV Kr^{+2} irradiated W-TiC (1.1%) sample at 1073 K showing a large TiC dispersoid with large voids on the interface with the W matrix.

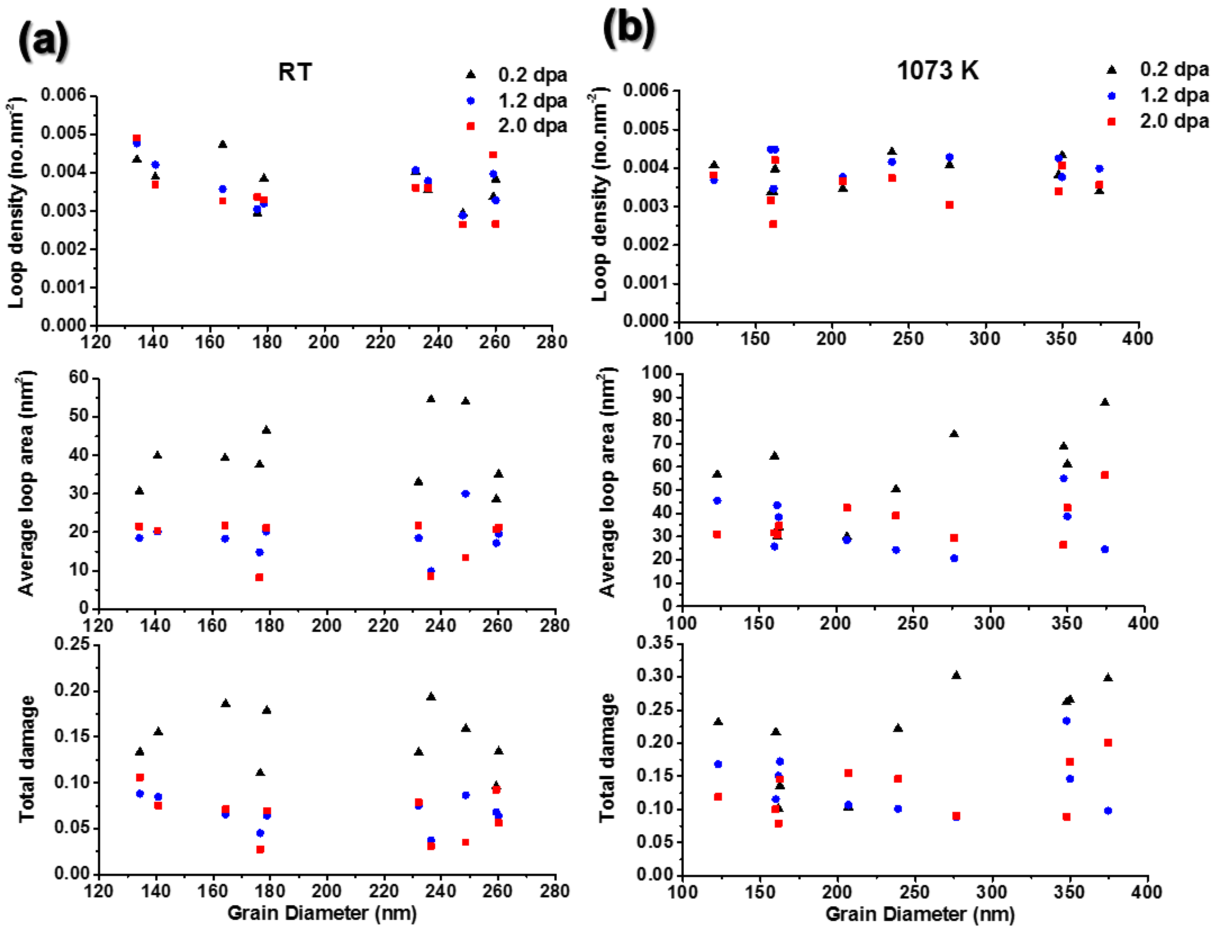

Figure 9: Average areal loop density, loop area and total damage as a function of grain size for several dpa values for the *in-situ* 1 MeV Kr^{+2} irradiated W-TiC (1.1%) samples at (a) RT and (b) 1073 K.

4. Discussion

4.1. Burgers vector type

The Burgers vector type of the dislocation loops formed during heavy ion irradiation of tungsten foils was previously investigated, and a discrepancy in literature results is observed. While Yi et al. [8] observed no <100> Burgers vectors in heavy ion irradiated tungsten foils at 1073 K, El-Atwani et al. [42] have shown that <100> Burgers vector loops exist at both RT and

1050 K during 3 MeV Cu^+ irradiation. These loops were demonstrated to be of small size and to occur directly from the collision cascade as vacancy-type loops [44], which grow when absorbing vacancies and can evolve into voids [45]. In this work, <100> loops were shown to exist and their density increased at 1073 K compared to RT. Due to the small size of the loops and the grains, it was not possible to perform the inside-outside contrast analysis to identify the nature of the individual loops formed. We acknowledge the fact that more grains have to be investigated in order to confirm this trend versus temperature (which is very challenging due to the small grain size of the samples), but also note that such a trend was also confirmed in BCC iron systems[46]. It is not expected, however, that tungsten will directly follow BCC iron behavior if the formation mechanisms of these loops in both materials are different.

4.2. Damage quantification and irradiation tolerance

4.2.1. Dislocation loop damage

The main goal of this work was to understand the radiation tolerance of the W-TiC (1.1%) alloys, which are particularly of interest due to their superior thermal stability and mechanical properties relative to pure tungsten [31, 34, 35]. In a previous study, W-TiC (0.5%) with ultrafine (100-500 nm) and nanocrystalline (<100 nm) microstructures were shown to be free of irradiation hardening when exposed to neutron irradiation at 873 K to a fluence of 2 x 10^{24} $n.m^{-2}$ with lower loop and void densities relative to pure tungsten [47]. W-TiC alloys have also been demonstrated to exhibit reduced blistering and retention when exposed to deuterium-helium plasma mixtures [48]. However, these irradiation studies were performed ex-situ and thus lacked dynamic observations to help distinguish the effects of alloying additions that lead to the formation of TiC dispersoids in the tungsten matrix from the reduction in grain size. The results presented herein were instead performed in-situ and thus, we were able to map the evolution of loop density, area, and total damage as a function of dose, which collectively provide new insights for understanding the radiation tolerance of the W-TiC (1.1%) alloys relative to pure tungsten as discussed below.

The loop density in Figure 6 was nearly identical for the samples irradiated at both RT and 1073 K, exhibiting an initial increase up to approximately 0.5 dpa and subsequent decrease. It is possible that this behavior could have resulted from loop coarsening, as previously observed in heavy ion irradiated tungsten and iron [42, 49]. However, the peak in the average loop area at approximately 0.3 dpa and subsequent decrease together indicate that loop coarsening did *not* account for the decrease in the loop density in this case. The loop area also exhibited an explicit temperature dependence where the loops formed during irradiation at 1073 K were generally larger than those formed at RT. The total damage followed the same trend as the average loop area, suggesting that the loop area governed the behavior after an initial incubation period in the W-TiC (1.1%) alloys. This indicates that, at high temperature, only changes in loop area govern the irradiation damage mechanism. According to established damage recovery stages in tungsten [6], 1073 K corresponds to stage IV (although still subject to controversy) and is above the temperature where monovacancies can move and recombine with interstitials (stage III) whereas RT corresponds to stage II where only interstitials (but not vacancies) can migrate [50] with small loops forming. Enhanced recombination of vacancies and interstitials are thus expected at elevated temperatures due to enhanced defect mobilities, which would tend to act to decrease the total damage, behavior that is contradictory to our defect evolution trends. However, in the W-TiC (1.1%) alloys, the situation is very complex due to the large number of potential defect sinks and second phase particles, and involves a wide variety of competing phenomena that can drive the damage response in opposing directions. These phenomena, grouped based on applicable temperature ranges, are summarized in Table 1.

Table 1: Complimentary and competing phenomena and their impact on irradiation damage

Temperature	***Phenomena***	***Consequence***	***Impact on Loop Damage***
Low T (interstitial migration only)	**Vacancy supersaturation**	Enhanced recombination due to increased vacancy concentration Decreased probability of recombination due to low vacancy mobility	Either increase or decrease in loop damage depending on the balance of probabilities influencing the total recombination rate
High T (interstitial and vacancy migration)	**Vacancy migration**	Enhanced recombination due to increased vacancy mobility Decreased probability of recombination due to reduced vacancy concentration	Either increase or decrease in loop damage depending on the balance of probabilities influencing the total recombination rate
	Vacancy annihilation at sinks (interfaces and existing loops)	Reduction in vacancy concentration leading to reduced probability of recombination	Decrease in vacancy loop damage accompanied by an increase in interstitial loop damage
	Vacancy loop transformation to voids	Void growth at the expense of defect loops	Suppression of loop damage at the expense of void growth
Low & high T	**High interstitial loop mobility**	Loop annihilation at surfaces Loop annihilation at defect sinks	Underestimation of loop damage (TEM foil effect) Decrease in loop damage
	Loop pinning by impurities and dispersoids	Reduced annihilation at sinks/surfaces Modification to point defect concentrations	Increase in apparent loop damage Increase or decrease depending on loop type (vacancy or interstitial)
	Grain boundary segregation	Augmented grain boundary sink efficiency	Increase or decrease in irradiation damage
	Defect interactions with sinks (interfaces and existing loops)	Neutral or biased sink behavior	Decrease in damage. If biased, can promote one type of loop damage (vacancy or interstitial)

As noted above, vacancies do not migrate at RT in tungsten [51] and consequently, the irradiated region can become saturated with immobile and dispersed vacancies. An interstitial may then have a higher probability to find a vacancy and recombine (rather than finding a sink), although the probability of recombination will also be limited by the low vacancy mobility at these temperatures. The degree of loop damage in the irradiated region will thus depend on the balance of probabilities influencing the total recombination rate. At high temperatures, vacancies are mobile and can diffuse to sinks including existing loops, grain boundaries, and dispersoid-matrix interfaces, which would act to decrease interstitial-vacancy recombination in the grain matrices at 1073 K. However, a number of complementary mechanisms are also activated at elevated temperatures that could lead to a suppression of loop density including surface defect annihilation (TEM foil effect), vacancy flux to support the growth of vacancy loops [45], and vacancy coalescence to form voids (though these are partially accounted for in the void count). All of the above mechanisms will be impacted by the presence of impurities and dispersoids, which act to pin the loops effectively reducing their mobility, and thus increase the probability of vacancy annihilation within loops at the expense of annihilation at sinks. We finally note that the influence of solute and impurity segregation on sink efficiency is still not well understood, but can potentially influence the damage state in the W-TiC (1.1%) alloys given their complex microstructure.

While the above discussion demonstrates that the response of the material is a convolution of many competing/complementary effects and isolating the dominant mechanism for any given condition is challenging, our in situ measurements provide useful insights into the underlying physics governing the radiation tolerance of the W-TiC (1.1%) alloys. Based on the consistent loop densities across both irradiation temperatures, the larger loop sizes at 1073 K, and prevalence of voids in the dispersoid-matrix interface, the greater total loop damage at 1073 K relative to RT is attributed to enhanced interstitial absorption by existing interstitial loops and vacancy absorption by vacancy loops. Three mechanisms are postulated to contribute to this effect, namely vacancies being biased to the dispersoid-matrix interfaces (promoting interstitial loop growth), reduced recombination of vacancies and interstitials (promoting interstitial and vacancy loop growth), and vacancy migration to vacancy loops (promoting vacancy loop growth). We note these mechanisms are consistent with the behavior in nanocomposite oxides containing heterointerfaces where damage accumulation can be enhanced if interstitials and vacancies preferentially migrate to different regions of the material (i.e. one prefers the interface while the other does not). [52]

4.2.2. Comparison with CGW (loop damage)

For comparison, pure tungsten irradiated at the same conditions as the W-TiC (1.1%) alloys at 1073 K is shown in Figure 10. Relative to the damage microstructures shown in Figure 4, the loops appeared significantly larger in CGW. Quantification of loop damage is depicted in Figure 11 and while loop density in W-TiC (1.1%) was initially larger, it converged with CGW at approximately 0.6 dpa after an initial incubation period. Despite these different loop densities during the onset of damage, the average loop areas were comparable below 0.3 dpa, resulting in enhanced loop damage initially in the W-TiC samples. However, after 0.3 dpa, the average loop area was much larger in CGW, thereby producing greater damage relative to the W-TiC (1.1%) alloy.

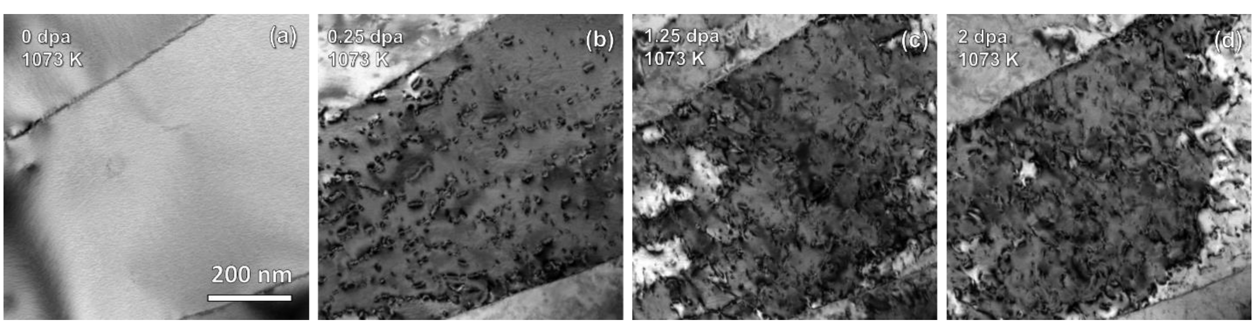

Figure 10: Bright-field TEM micrographs as a function of dpa for *in-situ* 1 MeV Kr^{+2} irradiated CGW sample at 1073 K (a) pre-irradiation, (b) 0.25 dpa, (c) 1.25 dpa, and (d) 2 dpa. The grain quantified (in the micrograph) has a size of ~ 650 nm.

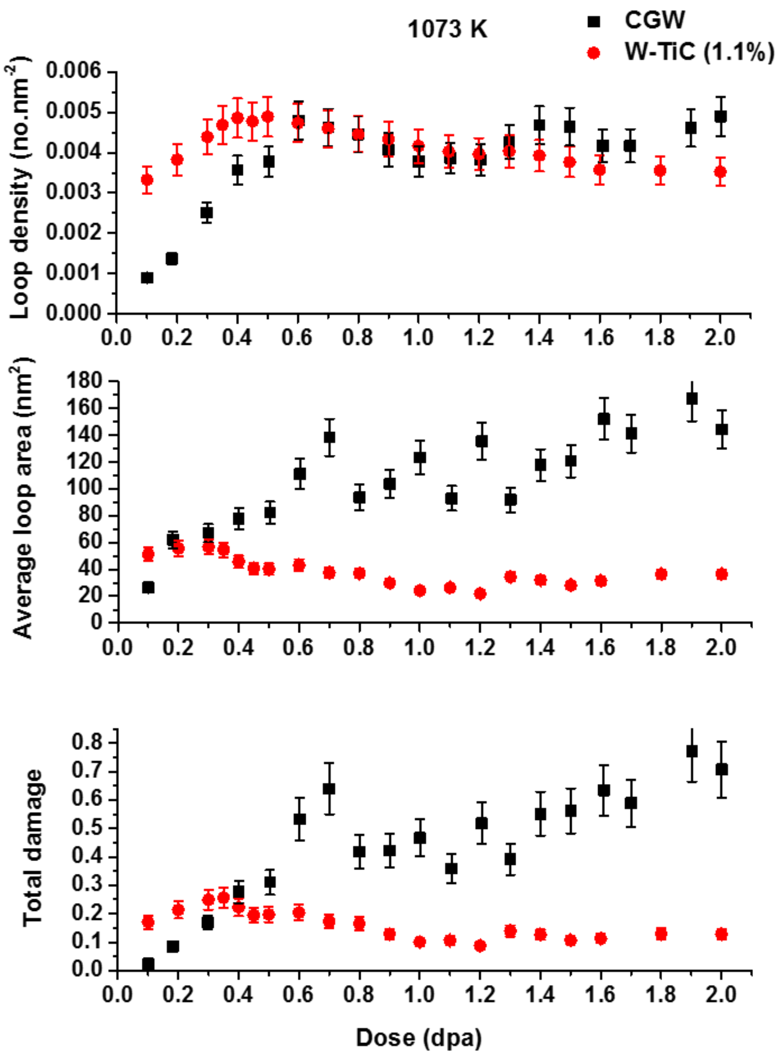

Figure 11: Comparisons of average areal loop density, loop area, and total damage (loop density × loop area) as a function of dpa for the *in-situ* 1 MeV Kr^{+2} irradiated CGW and W-TiC (1.1%) sample at 1073 K. Error bars are included to reflect errors in quantifying the same area several times.

With increasing dose, the total damage in CGW followed the average loop area due to the plateau of defect density, consistent with the W-TiC (1.1%) alloy. The loop area in CGW at the final dose of 2 dpa exhibited approximately 6 times greater total damage due primarily to the larger defect loop size. The grain sizes of CGW were on the order of ~ 650 nm, which was more than double the typical grain sizes in W-TiC (1.1%) sample. Taking into consideration surface effects (i.e., where surfaces act as defect and loop sinks), it is expected that the difference in irradiation damage between the CGW and the W-TiC samples will be even greater than what the loop damage trends indicate since the loop damage in CGW is underestimated by the presence of surfaces). The enhanced irradiation tolerance of W-TiC is mainly reflected in small loop sizes, which is due to enhanced interstitial and vacancy absorption at the interfaces (dispersoids and grain boundaries) as discussed in the previous section. From the TEM micrographs (Figures 4 and 10), it is evident that the W-TiC samples were more resistant to dislocation loop rafting (decoration of dislocation loops into parallel lines) [53, 54] which is expected considering the enhanced irradiation tolerance (lower loop density at 2 dpa) and the reduced loop mobility relative to CGW.

4.2.3. Comparison with CGW (void damage)

The degree of void damage in W-TiC (1.1%) at 1073 K (Figure 7) was compared with irradiated CGW. In CGW, the void density, average area, and corresponding change in volume were 0.1 void·nm^{-2}, 3.80 nm^2, and 0.55% respectively, all of which were higher than the W-TiC alloy and indicative of an enhanced resistance to void damage and swelling. Such enhancement can be attributed to the higher grain boundary density in the W-TiC sample and/or the presence of the alloying elements. While the enhanced resistance to void damage is consistent with pure nanocrystalline tungsten irradiated at 1073 K with 3 MeV Cu$^+$ reported by El-Atwani et al. [42], the grain sizes in the W-TiC (1.1%) alloy fell in the ultrafine regime the degree of irradiation damage was independent of grain size in pure nanocrystalline tungsten. In Figure 8, large voids (8-16 nm) were observed in the vicinity of the interface of a large TiC dispersoid and the grain matrix, indicating that these interfaces act as strong vacancy sinks. This suggests that the enhanced tolerance to void damage in W-TiC can be attributed to the presence of the dispersoid interfaces and consistent with observations in austenitic stainless steels containing TiC dispersoids, where the misfit between the particles and the matrix were proposed to aid in mutual defect recombination and absorption of excess vacancies. [55] We finally note that void shrinkage has previously been investigated in pure nanocrystalline tungsten as a function of dpa [42]; however, the degree of shrinkage can vary with dose and between the different grades of tungsten due to the presence of alloying elements and different grain boundary characteristics (i.e. volume fraction, misorientation distributions, and chemistry). A direct comparison of the W-TiC (1.1%) alloy with pure nanocrystalline tungsten necessitates a complete understanding of these effects and is thus beyond the scope of this study.

4.2.4. Damage evolution behavior

An important question we may examine using the in situ measurements is the difference in damage evolution behavior of the W-TiC (1.1%) alloy relative to pure tungsten and in particular, the inflection in loop density that was coincident with a decrease in the average loop size. Such behavior is generally not observed in pure ultrafine and nanocrystalline metals [17, 49]. In the absence of loop coalescence, average loop size can only increase via interstitial absorption. This suggests that the addition of TiC to tungsten played an important role in limiting the interstitial supply to existing loops through, e.g., the introduction of efficient defect sinks. In other words, the reduction in loop size in the W-TiC samples, which was absent in irradiated pure tungsten, suggests that the balance of interstitial and vacancy fluxes to the loops is different and the defect flux responsible for loop growth is smaller in W-TiC relative to pure tungsten. However, a decrease in loop size was also observed at RT when vacancies cannot migrate in tungsten, indicating that alternative mechanisms were responsible for the observed loop shrinkage. During in-situ irradiation, loop migration in the W-TiC sample irradiated at 1073 K transpired more rapidly as compared with pure tungsten (cf. videos S1 and S2 in the supplemental materials). If an interstitial loop encounters more vacancies than interstitials, slower moving loops can lead to an enhanced probability of vacancy annihilation and in turn, loop shrinkage and annihilation; an analogous argument can be made for vacancy loops that encounter more interstitials than vacancies.

The reduced loop migration rates can also render the loops stationary targets to collision cascades, which can lead to loop shrinkage via ballistic processes. Figure 12 (video S3 in the supplemental) shows bright-field TEM micrographs of large loops that shrank or were annihilated during irradiation without any change in the contrast of the grain (diffraction conditions) or position of the loops. Vacancy loop shrinkage has been previously observed in tungsten and was attributed to self-trapping of loops by long-range elastic fields and interactions with small interstitial loops.[56] Such interactions can be enhanced in the presence of impurities due to additional barriers for the thermal migration of loops (pinning or trapping effects). The shrinkage of larger loops can indeed be responsible for the observed decrease in the average loop size as a function of dose and is consistent with the decrease in the loop density following a peak damage state (Figure 5) as well as loop annihilation contributing to the enhanced void damage resistance in the W-TiC samples. The decrease in loop density can also derive from vacancy loop transformation to voids [45] during the course of irradiation, and the balance in these rates will ultimately dictate the dominant mechanism.

While the cyclic variations in the average loop area needs further detailed statistics to better quantify this behavior, it is consistent with the competition of several phenomena including the growth of existing loops (which would increase the average loop size), nucleation of new small loops (which would decrease the average loop size), annihilation of some loops by interfaces (which was rarely observed in the W-TiC alloys, but can increase or decrease the average size depending on the size of the loops annihilated), and the shrinkage or annihilation of some loops either by collision cascades or by annihilation with vacancies (which would decrease the average loop size). It should be mentioned here that the differences in grain boundary sink efficiencies can also affect the morphology evolution of the samples. Understanding the effect of impurities and possible segregation to the grain boundaries on the resulting sink strength and efficiency can assist in understanding the differences in radiation tolerance and loop behavior in the pure tungsten and the W-TiC alloys. In W-TiC both at RT and 1073 K, there is no apparent effect of the grain size on the damage evolution. However, grains with similar sizes and at the same dose showed different total damage values (up to 80 % change in the largest case). Since most grain boundaries in these alloys are high angle boundaries (Figure 2), such changes might be due to the effect of grain boundary plane or microstates [11, 57] as well as differing distributions and densities of impurities (from dispersoids) at different boundaries.

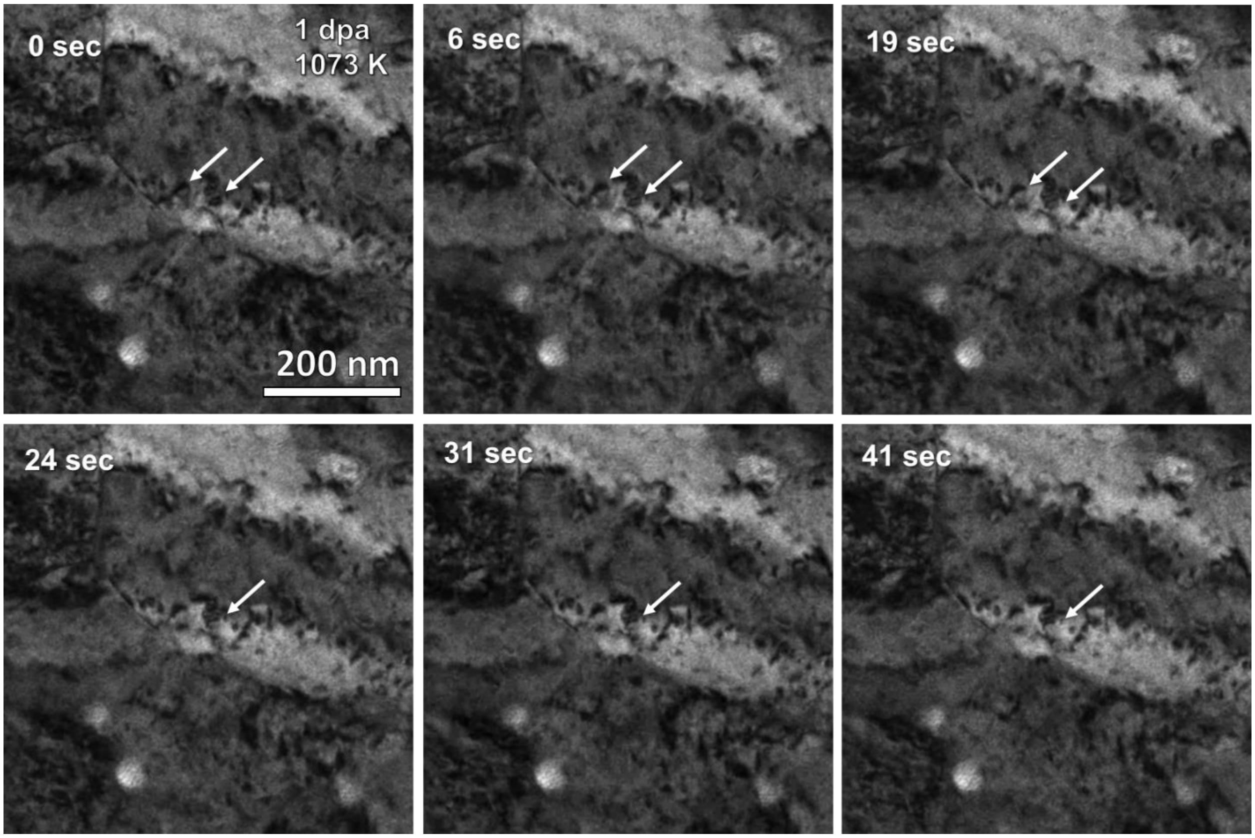

Figure 12: Snapshot bright-field TEM micrographs taken from a video (video S3 in the supplemental) at ~1 dpa showing loop shrinkage/annihilation in the W-TiC (1.1%) sample irradiated *in-situ* with 1 MeV Kr^{+2} at 1073 K.

5. Conclusions

In summary, in-situ TEM/irradiation was performed on thin foils of an ultrafine W-TiC (1.1%) alloy using 1 MeV Kr^{+2} irradiation at RT and 1073 K. The morphological evolution, as described by dislocation loop density, average loop area and total damage, was studied as a function of dose (dpa). The primary conclusions are as follows:

1- Dislocation loop density initially increased at low doses, which was followed by a peak at about 0.5 dpa and 0.4 dpa at RT and 1073 K, respectively, before decreasing and saturating (Figure 5).

2- The average loop area increased up to 0.3 dpa and then decreased (Figure 5), on average, with dose, though oscillating at higher doses, revealing an interesting behavior (loop area decrease) that has not been observed in pure materials. The total damage followed the same trend as the average loop area (a consequence of the fact that the density is constant versus dose at high dose).

3- Higher total loop damage was observed at 1073 K compared to RT (Figure 5), which was attributed to higher interstitial absorption of loops at 1073 K and biased sink behavior of the dispersoids as indicated by large voids at the interfaces between the dispersoids and the matrix (Figure 8).

4- Higher irradiation tolerance, as described by less total loop and void damage, was found in the W-TiC alloys relative to CGW at 1073 K. While the loop density in both grades was not significantly different, the average loop area in the W-TiC (1.1%) sample was much smaller and decreased with time while opposite scaling behavior was observed in CGW (Figure 11)

5- The decrease in loop area in the W-TiC alloy vs. dose was attributed to cascade damage (dissolution) of the loops and/or shrinkage of the loops (Figure 12) due to annihilation, both of which are enhanced due to the low mobility of the loops in these alloys (Videos S1, S2 and S3) . Collectively, the reduced loop mobility and enhanced irradiation tolerance of the W-TiC alloy improved the resistance of this alloy to raft formation.

6- There is no evident effect of grain size in the ultrafine regime on defect evolution (Figure 9), although grains with similar sizes showed distinct values of total damage. This is attributed to the effect of overall grain boundary character and density as well as distribution of dispersoids in different grains.

It is evident that the W-TiC alloys exhibited an enhanced radiation tolerance to overall loop and void damage as well as rafting relative to CGW. The small loop areas in the W-TiC alloy confirmed the effect of dispersoids and higher grain boundary density in annihilating defects. The in-situ nature of the experiments provided insights on possible mechanisms underpinning this behavior in the alloy; however, understanding the exact mechanisms responsible for the distinctive damage evolution behavior of the alloys and their implications for radiation tolerance requires further experimental and modeling studies directed towards individual phenomena rather than collective performance.

Acknowledgements

This work was supported by the U.S. Department of Energy, Office of Nuclear Energy under DOE Idaho Operations Office Contract DE-AC07- 051D14517 as part of a Nuclear Science User Facilities experiment. Research presented in this article was also supported by the Laboratory Directed Research and Development program of Los Alamos National Laboratory under project number 20160674PRD3. WSC and JRT acknowledge support for this work from the Department of Energy through Grant DE-SC0017899. We gratefully acknowledge the support of the U.S. Department of Energy through the LANL/LDRD Program and the G. T. Seaborg Institute for this work. BPU acknowledges support by the United States Department of Energy (US DOE) SciDAC program.

Figure Captions

Figure 1: (a) TEM bright-field micrograph of the as-received W-TiC (1.1%) sample showing TiC dispersoids on the grain boundaries as well as the grain matrices. Insert shows the diffraction pattern rings of pure W and TiC dispersoids. (b) Cross-section FIB image (using the secondary electrons of the gallium ion beam) showing no grain size or dispersoid density change with depth.

Figure 2: (a) EBSD [001] inverse pole-figure (IPF) map of the W-TiC (1.1%) sample, and (b), (c) the corresponding grain boundary map and TiC phase map respectively. (d), (e) Average grain size and grain boundary angle distributions respectively.

Figure 3: (a), (b) Bright-field 2-beam TEM micrographs using <110> g vector for the *in-situ* 2 dpa 1 MeV Kr^{+2} irradiated W-TiC (1.1%) samples at RT and 1073 K respectively. (c), (d)) Bright-field 2-beam TEM micrographs using <200> g vector for the 2 dpa irradiated W-TiC (1.1%) samples at RT and 1073 K respectively. Images are used to determine the percentages of <111> and <100> Burgers vectors (shown on the bottom of the figure) at RT and 1073 K. All micrographs have the same scale bar.

Figure 4: (a), (b), (c), (d) Bright-field TEM micrographs as a function of dpa for *in-situ* 1 MeV Kr^{+2} irradiated W-TiC (1.1%) sample at RT. (e), (f), (g), (h) Bright-field TEM micrographs as a function of dpa for the *in-situ* 1 MeV Kr^{+2} irradiated W-TiC (1.1%) sample at 1073 K. All micrographs have the same scale bar.

Figure 5: Comparisons of average areal loop density, loop area and total damage (loop density × loop area) as a function of dpa for the *in-situ* 1 MeV Kr^{+2} irradiated W-TiC (1.1%) sample at RT and 1073 K. Error bars are included to reflect errors in quantifying the same area several times. Note that the scales for average loop area and total damage are different in the two figures, with larger scales for the 1073 K irradiation.

Figure 6: Superimposed average areal loop density, loop area and total damage (loop density × loop area) as a function of dpa for the (a) RT and (b) 1073 K *in-situ* 1 MeV Kr^{+2} irradiated W-TiC (1.1%) sample. Error bars are included to reflect errors in quantifying the same area several times.

This is the same data as presented in Figure 5, but with the measurements for the two different temperatures superimposed for easier comparison.

Figure 7: Bright-field Fresnel (underfocus) TEM micrograph of 2 dpa *in-situ* 1 MeV Kr^{+2} irradiated W-TiC (1.1%) sample showing uniform distribution of voids (bright spots in the image). Average void density, void area and the corresponding swelling % extracted from this image are given at the bottom of the figure.

Figure 8: Bright-field TEM micrograph of the 2 dpa *in-situ* 1 MeV Kr^{+2} irradiated W-TiC (1.1%) sample at 1073 K showing a large TiC dispersoid with large voids on the interface with the W matrix.

Figure 9: Average areal loop density, loop area and total damage as a function of grain size for several dpa values for the *in-situ* 1 MeV Kr^{+2} irradiated W-TiC (1.1%) samples at (a) RT and (b) 1073 K.

Figure 10: Bright-field TEM micrographs as a function of dpa for *in-situ* 1 MeV Kr^{+2} irradiated CGW sample at 1073 K (a) pre-irradiation, (b) 0.25 dpa, (c) 1.25 dpa and (d) 2 dpa. The grain quantified (in the micrograph) has a size of ~ 650 nm.

Figure 11: Comparisons of average areal loop density, loop area and total damage (loop density × loop area) as a function of dpa for the *in-situ* 1 MeV Kr^{+2} irradiated CGW and W-TiC (1.1%) sample at RT and 1073 K. Error bars are included to reflect errors in quantifying same area several times.

Figure 12: Snapshots bright-field TEM micrographs taken from a video (video S3 in the supplemental) at ~1 dpa showing loop shrinkage/annihilation in the W-TiC (1.1%) sample irradiated *in-situ* with 1 MeV Kr^{+2} at 1073 K.

References

[1] B. Lipschultz, X. Bonnin, G. Counsell, A. Kallenbach, A. Kukushkin, K. Krieger, A. Leonard, A. Loarte, R. Neu, R. Pitts, Plasma–surface interaction, scrape-off layer and divertor physics: implications for ITER, Nuclear Fusion 47(9) (2007) 1189.
[2] V. Philipps, Tungsten as material for plasma-facing components in fusion devices, Journal of Nuclear Materials 415(1) (2011) S2-S9.
[3] S.J. Zinkle, L.L. Snead, Designing radiation resistance in materials for fusion energy, Annual Review of Materials Research 44 (2014) 241-267.
[4] J. Knaster, A. Moeslang, T. Muroga, Materials research for fusion, Nature Physics 12(5) (2016) 424-434.
[5] O. El-Atwani, J. Hinks, G. Greaves, S. Gonderman, T. Qiu, M. Efe, J. Allain, In-situ TEM observation of the response of ultrafine-and nanocrystalline-grained tungsten to extreme irradiation environments, Scientific reports 4 (2014).
[6] F. Ferroni, X. Yi, K. Arakawa, S.P. Fitzgerald, P.D. Edmondson, S.G. Roberts, High temperature annealing of ion irradiated tungsten, Acta Materialia 90 (2015) 380-393.
[7] X. Yi, M.L. Jenkins, K. Hattar, P.D. Edmondson, S.G. Roberts, Characterisation of radiation damage in W and W-based alloys from 2MeV self-ion near-bulk implantations, Acta Materialia 92 (2015) 163-177.
[8] X. Yi, M.L. Jenkins, M.A. Kirk, Z. Zhou, S.G. Roberts, In-situ TEM studies of 150 keV W+ ion irradiated W and W-alloys: Damage production and microstructural evolution, Acta Materialia 112 (2016) 105-120.
[9] O. El-Atwani, A. Suslova, T. Novakowski, K. Hattar, M. Efe, S. Harilal, A. Hassanein, In-situ TEM/heavy ion irradiation on ultrafine-and nanocrystalline-grained tungsten: Effect of 3MeV Si, Cu and W ions, Materials Characterization 99 (2015) 68-76.
[10] I. Beyerlein, A. Caro, M. Demkowicz, N. Mara, A. Misra, B. Uberuaga, Radiation damage tolerant nanomaterials, Mater. Today 16(11) (2013) 443-449.
[11] I. Beyerlein, M. Demkowicz, A. Misra, B. Uberuaga, Defect-interface interactions, Progress in Materials Science 74 (2015) 125-210.
[12] X.-M. Bai, A.F. Voter, R.G. Hoagland, M. Nastasi, B.P. Uberuaga, Efficient annealing of radiation damage near grain boundaries via interstitial emission, Science 327(5973) (2010) 1631-1634.
[13] T.D. Shen, S. Feng, M. Tang, J.A. Valdez, Y. Wang, K.E. Sickafus, Enhanced radiation tolerance in nanocrystalline MgGa 2 O 4, Applied physics letters 90(26) (2007) 263115-263115-3.
[14] N. Nita, R. Schaeublin, M. Victoria, Impact of irradiation on the microstructure of nanocrystalline materials, Journal of Nuclear Materials 329 (2004) 953-957.
[15] Y. Chimi, A. Iwase, N. Ishikawa, M. Kobiyama, T. Inami, S. Okuda, Accumulation and recovery of defects in ion-irradiated nanocrystalline gold, Journal of Nuclear Materials 297(3) (2001) 355-357.
[16] Y. Chen, J. Li, K. Yu, H. Wang, M. Kirk, M. Li, X. Zhang, In situ studies on radiation tolerance of nanotwinned Cu, Acta Materialia 111 (2016) 148-156.
[17] C. Sun, M. Song, K. Yu, Y. Chen, M. Kirk, M. Li, H. Wang, X. Zhang, In situ Evidence of Defect Cluster Absorption by Grain Boundaries in Kr Ion Irradiated Nanocrystalline Ni, Metallurgical and Materials Transactions A 44(4) (2013) 1966-1974.
[18] O. El-Atwani, J. Hinks, G. Greaves, J. Allain, S. Maloy, Grain size threshold for enhanced irradiation resistance in nanocrystalline and ultrafine tungsten, Materials Research Letters (2017) 1-7.
[19] O. El-Atwani, J. Nathaniel, A. Leff, B. Muntifering, J. Baldwin, K. Hattar, M. Taheri, The role of grain size in He bubble formation: Implications for swelling resistance, Journal of Nuclear Materials 484 (2017) 236-244.

[20] J. Li, K. Yu, Y. Chen, M. Song, H. Wang, M. Kirk, M. Li, X. Zhang, In Situ Study of Defect Migration Kinetics and Self-Healing of Twin Boundaries in Heavy Ion Irradiated Nanotwinned Metals, Nano Lett. 15(5) (2015) 2922-2927.
[21] S. Wurster, R. Pippan, Nanostructured metals under irradiation, Scripta Materialia 60(12) (2009) 1083-1087.
[22] M.A. Meyers, A. Mishra, D.J. Benson, Mechanical properties of nanocrystalline materials, Prog. Mater Sci. 51(4) (2006) 427-556.
[23] Q. Wei, T. Jiao, K. Ramesh, E. Ma, L. Kecskes, L. Magness, R. Dowding, V. Kazykhanov, R. Valiev, Mechanical behavior and dynamic failure of high-strength ultrafine grained tungsten under uniaxial compression, Acta Materialia 54(1) (2006) 77-87.
[24] Q. Wei, H. Zhang, B. Schuster, K. Ramesh, R. Valiev, L. Kecskes, R. Dowding, L. Magness, K. Cho, Microstructure and mechanical properties of super-strong nanocrystalline tungsten processed by high-pressure torsion, Acta materialia 54(15) (2006) 4079-4089.
[25] A. Ganeev, R. Islamgaliev, R. Valiev, Refinement of tungsten microstructure upon severe plastic deformation, The Physics of Metals and Metallography 115(2) (2014) 139-145.
[26] M. Efe, O. El-Atwani, Y. Guo, D.R. Klenosky, Microstructure refinement of tungsten by surface deformation for irradiation damage resistance, Scripta Materialia 70 (2014) 31-34.
[27] H.-Y. Guo, M. Xia, Z.-T. Wu, L.-C. Chan, Y. Dai, K. Wang, Q.-Z. Yan, M.-C. He, C.-C. Ge, J. Lu, Nanocrystalline-grained tungsten prepared by surface mechanical attrition treatment: Microstructure and mechanical properties, Journal of Nuclear Materials 480 (2016) 281-288.
[28] T. Chookajorn, H.A. Murdoch, C.A. Schuh, Design of stable nanocrystalline alloys, Science 337(6097) (2012) 951-954.
[29] O.K. Donaldson, K. Hattar, T. Kaub, G.B. Thompson, J.R. Trelewicz, Solute stabilization of nanocrystalline tungsten against abnormal grain growth, Journal of Materials Research 33(1) (2017) 68-80.
[30] Z.C. Cordero, E.L. Huskins, M. Park, S. Livers, M. Frary, B.E. Schuster, C.A. Schuh, Powder-route synthesis and mechanical testing of ultrafine grain tungsten alloys, Metallurgical and Materials Transactions A 45(8) (2014) 3609-3618.
[31] Y. Ishijima, H. Kurishita, H. Arakawa, M. Hasegawa, Y. Hiraoka, T. Takida, K. Takebe, Microstructure and bend ductility of W-0.3 mass% TiC alloys fabricated by advanced powder-metallurgical processing, Materials transactions 46(3) (2005) 568-574.
[32] H. Kurishita, Y. Amano, S. Kobayashi, K. Nakai, H. Arakawa, Y. Hiraoka, T. Takida, K. Takebe, H. Matsui, Development of ultra-fine grained W–TiC and their mechanical properties for fusion applications, Journal of nuclear Materials 367 (2007) 1453-1457.
[33] H. Kurishita, H. Arakawa, S. Matsuo, T. Sakamoto, S. Kobayashi, K. Nakai, G. Pintsuk, J. Linke, S. Tsurekawa, V. Yardley, Development of nanostructured tungsten based materials resistant to recrystallization and/or radiation induced embrittlement, Materials Transactions 54(4) (2013) 456-465.
[34] H. Kurishita, S. Matsuo, H. Arakawa, S. Kobayashi, K. Nakai, T. Takida, K. Takebe, M. Kawai, Superplastic deformation in W–0.5 wt.% TiC with approximately 0.1 μm grain size, Materials Science and Engineering: A 477(1-2) (2008) 162-167.
[35] S. Matsuo, H. Kurishita, H. Arakawa, T. Takida, M. Kato, Y. Yamamoto, K. Takebe, M. Kawai, N. Yoshida, Deformability enhancement in ultra-fine grained, Ar-contained W compacts by TiC additions up to 1.1%, Materials Science and Engineering: A 492(1-2) (2008) 475-480.
[36] Y. Kitsunai, H. Kurishita, H. Kayano, Y. Hiraoka, T. Igarashi, T. Takida, Microstructure and impact properties of ultra-fine grained tungsten alloys dispersed with TiC, Journal of Nuclear Materials 271 (1999) 423-428.

[37] H. Kurishita, S. Matsuo, H. Arakawa, M. Narui, M. Yamazaki, T. Sakamoto, S. Kobayashi, K. Nakai, T. Takida, K. Takebe, High temperature tensile properties and their application to toughness enhancement in ultra-fine grained W-(0-1.5) wt% TiC, Journal of Nuclear Materials 386 (2009) 579-582.
[38] J.F. Ziegler, M.D. Ziegler, J.P. Biersack, SRIM–The stopping and range of ions in matter (2010), Nuclear Instruments and Methods in Physics Research Section B: Beam Interactions with Materials and Atoms 268(11) (2010) 1818-1823.
[39] P. Jung, Atomic Defects in Metals (Landolt-Bornstein New Series III/25) ed H. Ullmaier, Berlin: Springer, 1991.
[40] O. El-Atwani, E. Esquivel, M. Efe, E. Aydogan, Y. Wang, E. Martinez, S. Maloy, Loop and void damage during heavy ion irradiation on nanocrystalline and coarse grained tungsten: Microstructure, effect of dpa rate, temperature, and grain size, Acta Mater. 149 (2018) 206-219.
[41] M. Jenkins, Characterisation of radiation-damage microstructures by TEM, Journal of nuclear materials 216 (1994) 124-156.
[42] O. El-Atwani, E. Esquivel, M. Efe, E. Aydogan, Y. Wang, E. Martinez, S. Maloy, Loop and void damage during heavy ion irradiation on nanocrystalline and coarse grained tungsten: Microstructure, effect of dpa rate, temperature, and grain size, Acta Materialia (2018).
[43] K. Yabuuchi, M. Saito, R. Kasada, A. Kimura, Neutron irradiation hardening and microstructure changes in Fe–Mn binary alloys, Journal of Nuclear Materials 414(3) (2011) 498-502.
[44] W. Setyawan, G. Nandipati, K.J. Roche, H.L. Heinisch, B.D. Wirth, R.J. Kurtz, Displacement cascades and defects annealing in tungsten, Part I: Defect database from molecular dynamics simulations, Journal of Nuclear Materials 462 (2015) 329-337.
[45] M. Gilbert, S. Dudarev, P. Derlet, D. Pettifor, Structure and metastability of mesoscopic vacancy and interstitial loop defects in iron and tungsten, Journal of Physics: Condensed Matter 20(34) (2008) 345214.
[46] G.A. Vetterick, Radiation Damage in Nanocrystalline Iron, DREXEL UNIVERSITY, 2014.
[47] H. Kurishita, S. Kobayashi, K. Nakai, T. Ogawa, A. Hasegawa, K. Abe, H. Arakawa, S. Matsuo, T. Takida, K. Takebe, Development of ultra-fine grained W–(0.25–0.8) wt% TiC and its superior resistance to neutron and 3 MeV He-ion irradiations, Journal of Nuclear Materials 377(1) (2008) 34-40.
[48] M. Miyamoto, D. Nishijima, Y. Ueda, R. Doerner, H. Kurishita, M. Baldwin, S. Morito, K. Ono, J. Hanna, Observations of suppressed retention and blistering for tungsten exposed to deuterium–helium mixture plasmas, Nuclear Fusion 49(6) (2009) 065035.
[49] O. El-Atwani, J. Nathaniel, A. Leff, K. Hattar, M. Taheri, Direct Observation of Sink-Dependent Defect Evolution in Nanocrystalline Iron under Irradiation, Scientific Reports 7 (2017).
[50] A. Debelle, M. Barthe, T. Sauvage, First temperature stage evolution of irradiation-induced defects in tungsten studied by positron annihilation spectroscopy, Journal of Nuclear Materials 376(2) (2008) 216-221.
[51] R.W. Balluffi, Vacancy defect mobilities and binding energies obtained from annealing studies, Journal of nuclear materials 69 (1978) 240-263.
[52] B. Pedro Uberuaga, E. Martinez, Z. Bi, M. Zhuo, Q. Jia, M. Nastasi, A. Misra, A. Caro, Defect distributions and transport in nanocomposites: a theoretical perspective, Materials Research Letters 1(4) (2013) 193-199.
[53] E.A. O. El-Atwani, E. Esquivel, M.Efe, Y. Wang, S.A. Maloy, Detailed transmission electron microscopy study on the mechanism of dislocation loop rafting in tungsten, Acta Materialia (2018).
[54] V. Sikka, J. Moteff, “Rafting” in neutron irradiated tungsten, Journal of Nuclear Materials 46(2) (1973) 217-219.
[55] W. Kesternich, J. Rothaut, Reduction of helium embrittlement in stainless steel by finely dispersed TiC precipitates, Journal of Nuclear Materials 104 (1981) 845-852.
[56] D. Mason, X. Yi, M. Kirk, S. Dudarev, Elastic trapping of dislocation loops in cascades in ion-irradiated tungsten foils, Journal of Physics: Condensed Matter 26(37) (2014) 375701.

[57] W. Han, M. Demkowicz, E. Fu, Y. Wang, A. Misra, Effect of grain boundary character on sink efficiency, Acta materialia 60(18) (2012) 6341-6351.